Aerospace Science and Technology 96 (2020) 105520

Contents lists available at ScienceDirect

Aerospace Science and Technology

www.elsevier.com/locate/aescte

Determination of optimal spacing between transverse jets in a SCRAMJET engine

Vatsalya Sharma [a], Vinayak Eswaran [a,*], Debasis Chakraborty [b]

[a] Department of Mechanical and Aerospace Engineering, Indian Institute of Technology, Hyderabad, India
[b] Directorate of Computational Dynamics, Defence Research and Development Lab, Hyderabad, India

ARTICLE INFO

Article history:
Received 22 October 2019
Received in revised form 25 October 2019
Accepted 27 October 2019
Available online 31 October 2019

Keywords:
SCRAMJET engine
RANS
Transverse sonic injection
Supersonic crossflow

ABSTRACT

A SCRAMJET engine typically has multiple transverse fuel injectors with a flame holder. In this study, we consider a two-jet SCRAMJET engine design configuration that uses the low speed recirculation region created by a backward facing step as a flame holder. The effect of spacing between the transverse fuel injectors on the performance of a SCRAMJET engine has been studied using cold-flow simulations. The position of the leading jet is kept fixed at the end of the recirculation zone as suggested by previous studies and the second jet is placed at various locations downstream in the distinct flow regions formed behind the leading jet. It is assumed that the two jets are identical in dimensions and flow. The spacing between the jets is expected to play a significant role in determine the performance of the SCRAMJET engine. Three-dimensional simulations have been performed, using Menter's SST model in our in-house parallel 3-D RANS unstructured grid CFD solver. The mixing of inlet air and the injected air-fuel in such a SCRAMJET configuration is augmented by the interaction of the transverse under-expanded jet with the incoming supersonic cross-flow through the generation of strong streamwise vorticity. The performance and mixing of the combustor have been quantified for each of the distinct configurations. It is observed that they are indeed affected by the spacing between the jets. From the results presented in this paper, the optimal location for the second jet is at the end of the zone over which the lateral momentum of the first jet is dominant in affecting the jet penetration into the streamwise flow.

1. Introduction

Transverse fuel injectors are a simple, reliable and conventional method to achieve rapid mixing of air and fuel stream in a SCRAMJET engine [1–3]. Since a SCRAMJET engine operates at very high speeds, the flame-holding and stabilization in such a flow field becomes a very critical issue, which can be solved by placing a backward facing step in the SCRAMJET combustor [4–10] to act as a flame-holder. The backward facing step creates a large recirculation zone, with the hot gases contained therein, that acts as a continuous ignition zone. Multiple injectors are placed in the downstream of the step to increase the thrust produced by the SCRAMJET engine. But in such a configuration, overall performance and mixing efficiency is dependent on a wide range of geometrical parameters such as the location and orientation of the injector, the angle of injection and the spacing between the injectors, to name a few.

Thus the study of the optimal spacing between the injectors is important in the design and performance of the SCRAMJET engine. Several studies have been performed to investigate the role of multiple injectors in the mixing of a transverse sonic jet in a supersonic crossflow for various configurations [11–13], but to the best knowledge of the authors, no study has been performed to investigate the optimal spacing between the consecutive injectors in a SCRAMJET engine configuration.

The objective of this study is to analyze the effect of the distance between the two consecutive jets on the overall performance, using various parameters to quantify mixing and flow physics. In order to conduct this study, 3-D RANS simulations of the SCRAMJET configuration used in Sharma et al. [14] have been performed on our in-house unstructured grid parallel 3D RANS solver. It has been previously reported [15–17] that the mixing of the jet and the incoming flow is decoupled from combustion, as the mixing of air-fuel streams are not strongly affected by the chemical kinetics and subsequent heat release through combustion in the supersonic flow field. Therefore, a cold flow analysis of the flow field could be used, at-least as a first approximation, to optimize the design of a SCRAMJET engine based on mixing considerations alone.

* Corresponding author.
E-mail address: eswar@iith.ac.in (V. Eswaran).

https://doi.org/10.1016/j.ast.2019.105520
1270-9638/

The optimal region for placing the leading jet in such a SCRAMJET engine configuration has been previously determined by Sharma et al. [14] to be the point of reattachment or slightly before, at the end of the recirculation region behind the step. In this study, we shall assume the first jet is placed at the reattachment point. To determine optimal spacing between the injectors, the second injector is placed in downstream of the first jet in each of the three distinct flow regions that are formed downstream of the leading transverse sonic injection [14]. The combustor design is then evaluated on the basis of better mixing of air-fuel and on other bases of performance. To quantify the mixing of fuel and air, we study the jet spread, penetration, effect of streamwise vorticity, and mixing efficiency. To quantify the performance of the SCRAMJET engine, the increase in entropy and stagnation pressure loss are evaluated and compared between the different cases. More than the mere numerical distance, emphasis has been laid on identifying the region where the leading jet should be placed, so as to find a common principle for different jet-to-free-stream pressure ratios.

2. Numerical method

The details of the in-house parallel three-dimensional unstructured grid RANS solver are given in this section.

2.1. Governing equation

The density based finite volume solver uses a low-speed preconditioned form of the Navier-Stokes equation [18] that allows its use for both the compressible and incompressible flow regimes. The solver can handle three-dimensional unstructured grids in CFD General Notification System (CGNS) format. The equation of state for an ideal gas is used:

$$p = \rho R T \tag{1}$$

where ρ, T, and P are the density, temperature and pressure of the fluid, respectively and R is the universal gas constant taken as $287\,JKg^{-1}K^{-1}$. The velocity vector is written as:

$$\mathbf{V} = u\hat{\mathbf{i}} + v\hat{\mathbf{j}} + w\hat{\mathbf{k}} \tag{2}$$

The integral form of the governing equation used, with control volume V and elemental face area $\mathbf{d}S$, is given as:

$$\Gamma \frac{\partial}{\partial t}\int_V \mathbf{Q}dV + \oint [\mathbf{F} - \mathbf{G}]\cdot d\mathbf{G} = \int_V \mathbf{H}dV \tag{3}$$

where $\mathbf{Q}$ is the primitive variables vector given as:

$$\mathbf{Q} = \{P, u, v, w, T\}^T \tag{4}$$

The magnitude of the face area $\mathbf{S}_f$ is A_f and its unit normal vector is $\hat{\mathbf{n}}_f$. In the governing equation (3), $\boldsymbol{G}$ is the diffusion vector and $\boldsymbol{F}$ is the convective vector of the compressible Navier-Stokes equation which are defined as:

$$\mathbf{F} = \begin{Bmatrix} \rho\mathbf{V} \\ \rho\mathbf{V}u + P\hat{\mathbf{i}} \\ \rho\mathbf{V}v + P\hat{\mathbf{j}} \\ \rho\mathbf{V}w + P\hat{\mathbf{k}} \\ \rho\mathbf{V}E + P\mathbf{V} \end{Bmatrix}, \quad \mathbf{G} = \begin{Bmatrix} 0 \\ \tau_{xi} \\ \tau_{yi} \\ \tau_{zi} \\ \tau_{ij}\mathbf{V}_j + \mathbf{q} \end{Bmatrix} \tag{5}$$

Here E and H are the total energy and total enthalpy per unit mass.

$$E = H - \frac{p}{\rho} \quad ; \quad H = h + |\mathbf{V}|^2/2 \tag{6}$$

and $\mathbf{q}$ is the heat flux vector:

$$\boldsymbol{q} = -k'\frac{\partial T}{\partial x_j} \tag{7}$$

where k' is the thermal conductivity of the fluid, and $\boldsymbol{\tau}$ is the viscous stress tensor:

$$\tau_{ij} = -P\delta_{ij} + \mu_L\left(\frac{\partial U_i}{\partial x_j} + \frac{\partial U_j}{\partial x_i}\right) + \lambda(div\mathbf{V})\delta_{ij} \tag{8}$$

where λ is the coefficient of bulk viscosity, determined using Stokes' hypothesis [19] and μ_L is the laminar dynamic viscosity of the fluid. In equation (3), Γ is the low speed preconditioning matrix that helps in getting convergence for incompressible flows with the density based algorithm [18]:

$$\Gamma = \begin{bmatrix} \Theta & 0 & 0 & 0 & \rho_T \\ \Theta u & \rho & 0 & 0 & \rho_T u \\ \Theta v & 0 & \rho & 0 & \rho_T u \\ \Theta w & 0 & 0 & \rho & \rho_T u \\ \Theta H - \delta & \rho u & \rho v & \rho w & \rho_T H + \rho C_p \end{bmatrix} \tag{9}$$

where,

$$\Theta = \left(\frac{1}{U_r^2} - \frac{\rho_T}{\rho C_p}\right), \; \rho_p = \left.\frac{\partial\rho}{\partial P}\right|_T, \; \rho_T = \left.\frac{\partial\rho}{\partial T}\right|_P \tag{10}$$

In equation (10), U_r is the reference velocity and δ is a constant of preconditioning, whose definitions can be found in Weiss et al. [20]. The vector $\boldsymbol{H}$ in the equation (3) contains source terms for body forces and energy sources, which have been set as 0 in this work. The 2nd order Roe scheme [21], preconditioned for low speeds [20] has been used for modeling the convective vector $\boldsymbol{F}$ of the governing equation with the Venkatkrishnan limiter [22,23]. The gradients in the diffusion vector $\boldsymbol{G}$ are computed using the Green-Gauss cell based method.

Explicit time-stepping is used to march the solution to steady-state using the 4th order Runga Kutta method on the governing equations. The time step Δt is computed from the CFL (Courant-Friedrichs-Lewy) condition. The same time step Δt is used in each cell of the domain. The residue e of each variable solved is stored and is checked for convergence independently:

$$e = \sqrt{\frac{1}{\Delta t}\sum_{cells}\left(\mathbf{Q}^{n+1} - \mathbf{Q}^{n}\right)} \tag{11}$$

Normalization with the initial residual is used to ensure that the initial residuals for all equations are of $O(1)$, which is quite useful in judging overall convergence. Further details of the method and the equations can be found in Sharma et al. [24].

2.2. Turbulence modeling

The SST k-ω two-equation model of Menter [25] in its low Reynolds number form is used in this study. The model equations for the turbulent kinetic energy k are:

$$\frac{\partial(\rho k)}{\partial t} + \frac{\partial(\rho U_j k)}{\partial x_j} = P_k - \beta^*\rho\omega k + D_k \tag{12}$$

For the specific dissipation $\omega(=\epsilon/C_\mu k)$

$$\frac{\partial(\rho\omega)}{\partial t} + \frac{\partial(\rho U_j\omega)}{\partial x_j} = \gamma'\frac{\omega}{k}P_k - \beta\rho\omega^2 + D_\omega + AA \tag{13}$$

where P_k is the production of turbulent kinetic energy evaluated as:

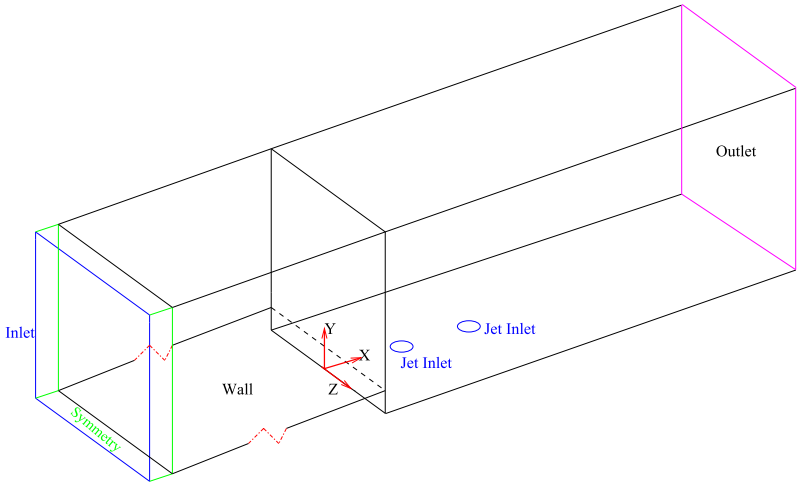

Fig. 1. Isometric view of the domain.

$$P_k = \tau_{ij} \frac{\partial U_j}{\partial x_i} \tag{14}$$

The rest of the model constants and definitions are as given by Menter [25]. The value of the laminar Prandtl number is taken as 0.71 and the turbulent Prandtl number (Pr_T) is taken as 0.9.

2.3. Passive scalar tracking to determine mixing

A convection-diffusion equation is also solved coupled with the system of governing equations in order to track mixing of the injected jet with the main air flow. For a passive scalar ϕ, the governing equation can be given as:

$$\frac{\partial \rho\phi}{\partial t} + \frac{\partial}{\partial x_i}(\rho\phi u_i) = \frac{\partial}{\partial x_i}\left(\rho\Gamma \frac{\partial}{\partial x_i}\phi\right) + S_\phi \tag{15}$$

where ρ is the density of the fluid, u_i is the component of the fluid velocity vector V and S_ϕ is the source term (which is set as 0 here), and Γ is the diffusivity for the scalar, given as:

$$\Gamma = \Gamma_k + \Gamma_t \tag{16}$$

where Γ_k is the molecular diffusivity with a value taken equal to the kinematic viscosity of the fluid, while the turbulent eddy diffusivity Γ_t is evaluated as:

$$\Gamma_t = \frac{\mu_t}{Sc_t} \tag{17}$$

where μ_t is turbulent viscosity obtained from the solver, and the value of the turbulent Schmidt number (Sc_t) is taken as 0.9.

The scalar ϕ is the *"mixing fraction"* that is given the value of 1 in the two fuel jet streams and 0 in the air inlet stream. As the fuel stream and air stream mix, we get values of ϕ between 0 and 1. The value of ϕ at a point in the flow will indicate the amount of mixing of the fuel and air streams, with $\phi = 1$ indicating unmixed fuel steam and 0 unmixed air stream and, say $\phi = 0.4$ indicating a 40% fuel stream and 60% air stream mixture (by mass). In practice, the fuel stream would be say, a kerosene-air mixture, which for convenience we take in this study to have the same properties as air.

3. Numerical validation and verification of the solver

The RANS solver is validated for benchmark cases to establish its capabilities and accuracy in the following sub-section.

Table 1
Domain dimensions.

Parameter	Value
Injector Diameter (D)	1.93 mm
Leading Injector Location	0, 0, 0
L_1	$56.0D$
L_2	$31.0D$
L_3	$4.94D$
W	$31.0D$
H	$15.8D$
Step location	$-4.94D$

3.1. Transverse sonic injection in supersonic cross flow over backward facing step

Experimental results obtained using Laser Induced Iodine Fluorescence (LIIF) by McDaniel et al. [4] to study the penetration and spread of dual staged transverse sonic jet in a supersonic cross flow over a backward facing step have been used as validation test case for our solver. The 3-D isometric view of the computational domain, along with boundary section names is shown in Fig. 1. Fig. 2 shows the 2-D views in the planes parallel and normal to the injectors, with the required dimensions being given in Table 1. Note that a line break has been used in the length of L_1 to fit the image.

Meshes have been constructed using the ICEM-CFD software and exported in the CGNS format. Unstructured 3-D meshes with quadrilateral elements at the boundary section and hexahedral elements in the interior computational domain have been used. Fig. 3 shows the mesh distribution in the computational domain.

In order to optimize the number of cells in the mesh, hyperbolic and exponential laws for node distribution have been used at different sections. Use of hexahedral cells in the mesh allows us to exert greater control over the grid stretching, refinement and an overall better quality of the mesh. Nodes are clustered near the leading edge of the inlet section to capture the effect of the shock generated by the leading edge of the inlet. Since, SST is a low-Reynolds number model, $y^+ < 1$ is required for all the grid point nearest to the wall, which has been ensured for all the walls in the computational domain. Therefore, the grid is stretched in the wall-normal direction using the hyperbolic law, as seen in Fig. 3a. The node distribution is refined selectively at the jet inlet as shown in Fig. 3c, using the hyperbolic mesh law to capture the most important flow features. Fig. 3b shows the exponential

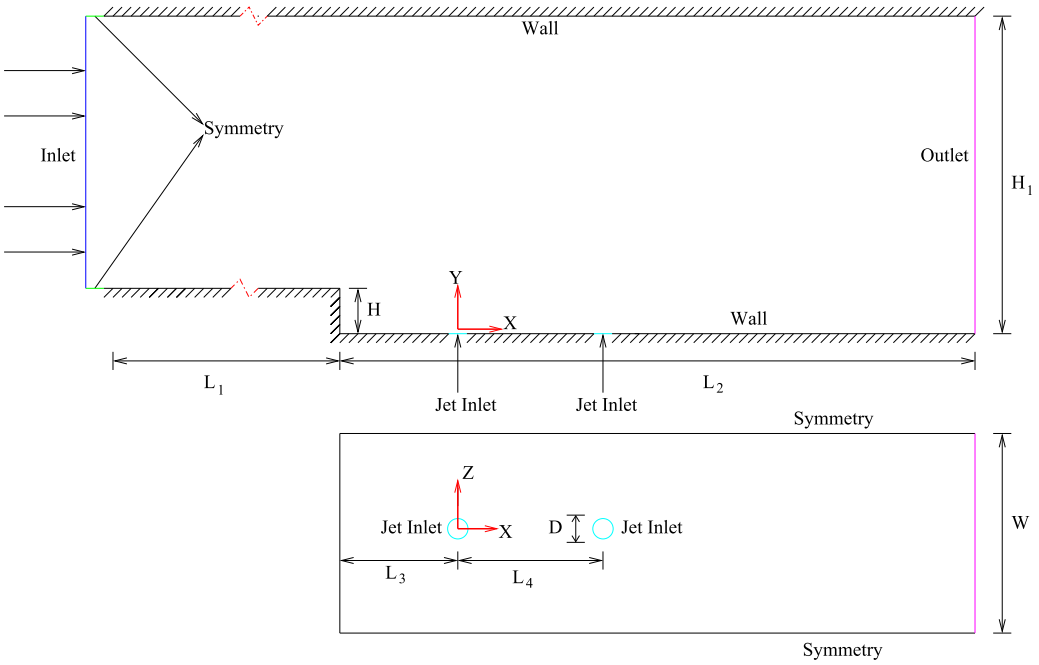

Fig. 2. Geometry for simulations and its boundary conditions.

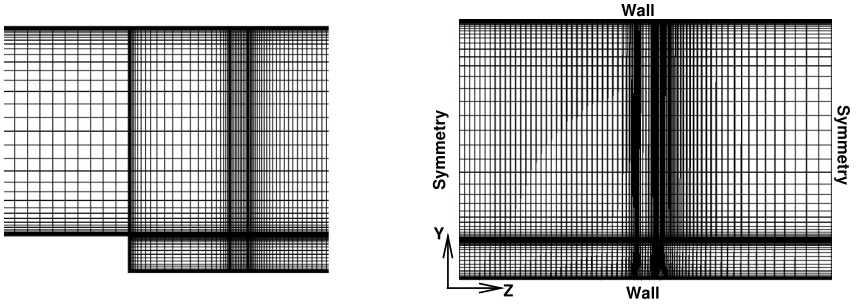

(a) Mesh distribution in the domain in X-Y plane

(b) Meshing in Y-Z plane as seen from the outlet section.

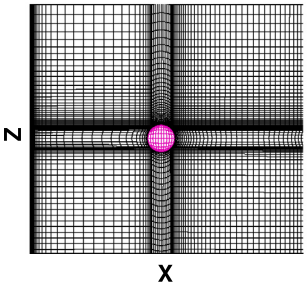

(c) Mesh distribution around the injector.

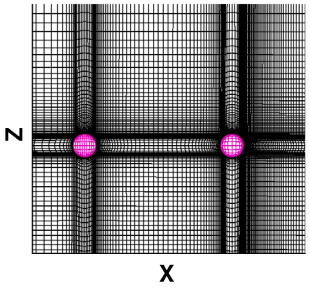

(d) Mesh distribution between the injectors.

Fig. 3. Mesh distribution.

mesh distribution used in the Z direction, with more nodes biased towards the center-plane of the computational domain. A symmetry boundary condition is prescribed on the boundary sections in the Z-plane. At-least 30% of the nodes in the transverse direction to any wall are concentrated in the region between the wall and a distance three times the jet diameter. Fig. 3d shows the grid spacing between the two injectors, using a hyperbolic mesh law for node distribution. In the region between the second injector and the outlet of the computational domain, the mesh is distributed using the exponential law, with more number of nodes biased towards the jet inlet. For a free-stream Mach number (M_∞) of 2.05 at the inlet, a pressure inlet boundary condition has been prescribed, with total pressure (P_t) = 274000 Pa, static temperature (T_{static}) = 163 K and total temperature (T_t) of 250 K. The wall is assumed as adiabatic, so $\mathbf{U} = 0$, $\frac{\partial T}{\partial n} = 0$, $\frac{\partial P}{\partial n} = 0$, $\frac{\partial \tilde{\nu}}{\partial n} = 0$ have been prescribed as boundary conditions there. At outflow, $\frac{P_t}{P_\infty} = 1$ has been prescribed, the remaining quantities are taken from interior values. Symmetry boundary conditions are prescribed in the Z direction. For all the sections labeled as symmetry, $\frac{\partial \mathbf{Q}}{\partial n} = 0$ has been prescribed. Since the injection is done at sonic speed, choked flow

Table 2
Boundary conditions (BC) for turbulence variables and passive scalar.

Section name	SST BC	Scalar (ϕ) BC
Inlet	$I = 5\%$	$\phi = 0$
Adiabatic Wall	$k = 0$ $\omega = 0$	$\phi = 0$
Outlet	$\frac{\partial k}{\partial n} = 0$ $\frac{\partial \omega}{\partial n} = 0$	$\frac{\partial \phi}{\partial n} = 0$
Symmetry	$\frac{\partial k}{\partial n} = 0$ $\frac{\partial \omega}{\partial n} = 0$	$\frac{\partial \phi}{\partial n} = 0$
Transverse Jet Inlet	$\frac{\partial k}{\partial n} = 0$ $\frac{\partial \omega}{\partial n} = 0$	$\phi = 1$

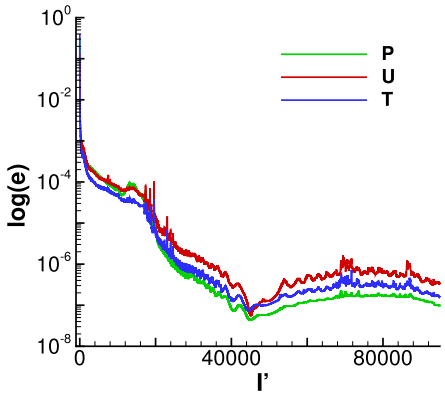

Fig. 4. Convergence.

conditions are prescribed at the jet inlet. The inlet jet dynamic pressure ratio (Q) is given as:

$$Q = \frac{1}{M_\infty^2} \frac{P_{jet}}{P_\infty} \tag{18}$$

where P_{jet} is the injected jet static pressure and P_∞ is the free stream static pressure. Simulations were performed for $Q = 1.05$ and compared with the experimental results of McDaniel et al. [4]. The jet penetration and spread is measured using the value of the passive scalar (ϕ). The boundary conditions for the turbulent variables and for ϕ are given in Table 2.

Explicit time stepping using Ranga-Kutta 4th order scheme as described in Sharma et al. [24] with CFL numbers ranging between 0.1–0.15 are used for the simulation. The solution is considered converged once the normalized velocity, pressure and temperature residuals are below $1e^{-6}$ and turbulent variables' residuals are below $1e^{-3}$ (see Fig. 4). The *jet penetration* is obtained by extracting the contour of $\phi = 1\%$ on the X-Y mid plane of the domain. The *jet spread* is obtained by extracting the same contour of $\phi = 1\%$ at the Y-Z plane located at a distance $Y/D = 1$ above the injector.

3.1.1. Grid independence study

Grid sensitivity study was done with three grids of size $N_1 = 3256500$, $N_2 = 399822$ and $N_3 = 48291$ using the Grid Convergence Index (GCI) [26], where N represents the total number of cells in the mesh. Fig. 5 shows the comparison of the jet penetration for $Q = 1.05$ using these three grids. The GCI analysis was done on the computed values of the jet penetration on the grids. On the finest grid, the empirical order of accuracy (p_{avg}) was obtained around 2.05 and maximum GCI, indicating the uncertainty, was obtained as 3.89%. Fig. 5b shows the jet penetration on the finest grid along with GCI error bars. Hence, the 3-D grid with 3256500 hexahedral cells is selected for the further computations. Using the N_1 grid, the penetration and spread is compared against the experimental results of McDaniel et al. [4] as shown in Fig. 6. A good match is seen to be obtained.

4. Results

Injecting a transverse sonic jet in the incoming supersonic cross-flow in a SCRAMJET engine creates various flow regions in its downstream, which have been studied in detail by Sharma et al. [14]. The location of the first jet at $L_3 = 4.94D$ is at the end of the recirculation zone behind at the step for the chosen flow conditions. We choose the center of the first jet as the origin $X/D = 0$ of the streamwise coordinate. Fig. 7 by Sharma et al. [14] shows the jet penetration when only the single transverse sonic jet located at $X/D = 0$ operates in the domain shown in the Fig. 1. In this paper, this case shall referred to as the *baseline case*. In Fig. 7, the region from A' to A represents the flow preceding the injector. A sharp rise in the value of jet penetration between A and B can be observed, which signifies that the jet penetration in this region is dominated by the transverse momentum of the jet, which exists till $X/D \approx 3$. The interaction of the fuel jet with the shocks and expansion waves created by the incoming supersonic cross-flow results in a strong baroclinic torque, which leads to formation of the counter rotating vortices [14], resulting in strong mixing in the aforementioned region. The abrupt rise in the penetration value at the jet $X/D = 0$ is due to the lateral momentum of the jet. The penetration boundary falls slightly after the location B ($X/D \approx 3.3$), and then begins to rise at point C ($X/D \approx 8$). After point C, the penetration boundary rises slowly, essentially by diffusion as the jet momentum has been expended, till the end of the graph at D. The penetration increases linearly in this diffusion zone. The region between points B and C represents the transition of the flow from being dominated by jet momentum to the diffusion dominated region of the mixing region. For the sake of convenience we label the three regions as the "momentum zone", "intermediate zone" and "diffusion zone" with reference to the Fig. 7. It is mentioned however that the flow always is strongly convective in the streamwise direction.

In order to investigate the optimal location for the follow-up jet, the leading injector is kept fixed at $X/D = 0$ and the second injector is then placed in each of the following locations in the flow regions shown in Fig. 7:

1. Case A: "Momentum zone" $X/D = 3.3$.
2. Case B: "Transition zone" $X/D = 6.6$.
3. Case C: "Diffusion zone" $X/D = 12.8$.

For each case, the length L_4 in Fig. 2 is varied accordingly. The number of nodes on L_4 and L_5 are redistributed for each of the 3 cases, in order to keep the total number of cells constant across all the cases. The local distribution of nodes around the injector and for the remaining directions is maintained as stated in Sec. 3.1. For the sake of comparison, all the simulations in this section have been done at a fixed $Q = 1.05$, with the same computational domain, boundary conditions and convergence criteria as described in Sec. 3.1. The total mesh size for each case is 3256500 hexahedral cells.

4.1. Overview of the flow field

Key features of the flow-field with two fuel injectors is been shown are Fig. 8. The figure consists of two parts. The upper half of the figure consists of the P_{norm} isobars with Mach number contours, whereas in the lower part the contours of mixing fraction ϕ with streamlines are shown. The plots are of the mid-X-Y plane of the combustor domain. From this figure, it is observed that the supersonic flow turns over the sharp corner of the backward facing step causing the turbulent boundary layer to separate. The flow then turns downwards over the step, resulting in formation of a Prandtl-Meyer Expansion Fans (PMEF) after the step. The separated

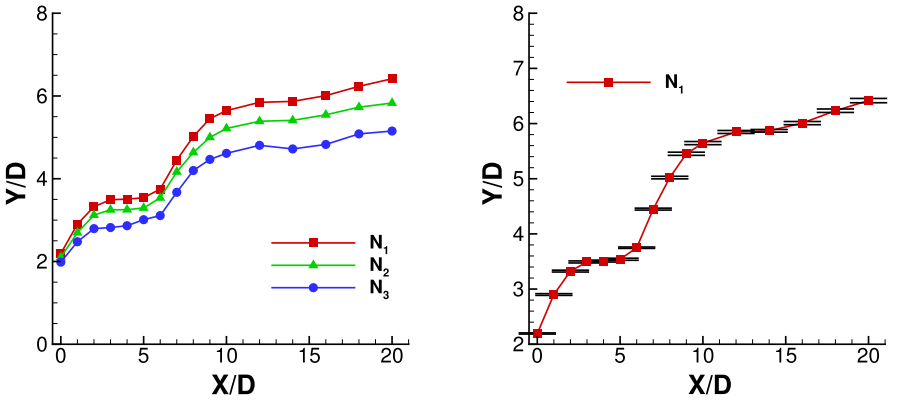

Fig. 5. GCI of jet penetration.

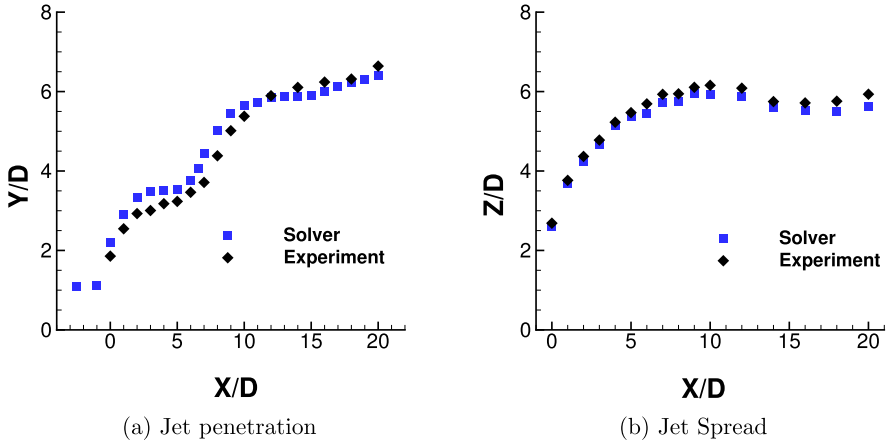

Fig. 6. Comparison of jet penetration and spread against experiments done by McDaniel et al. [4] on finest N_1 grid.

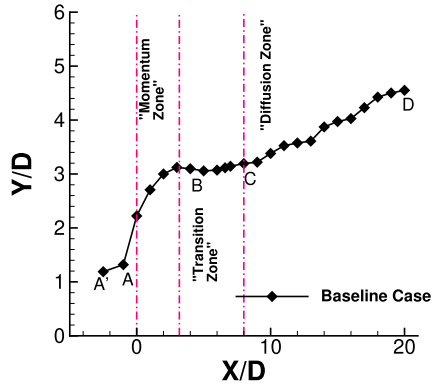

Fig. 7. Flow regime description for the baseline case.

flow then curves downwards to subsequently impinge on the bottom wall, thus forming a recirculation zone. The fuel is injected at the sonic speed into the combustor from the two injectors that are placed in-line in the downstream of the step, as shown in Fig. 2. It should be noted that both the injectors are exactly same in dimensions and mass flow-rate at the sonic conditions. When the air stream encounters the under-expanded jet from the first injector, a strong bow shock is created, with a small upstream separation bubble. The shock waves generated by the jet and the PMEFs at the step together create a region of strong lateral convection near the first injector. The interaction of the bow shock with the fuel jet leads to the creation of baroclinic torque, which then results in the formation of a counter-rotating vortex pair in the streamwise direction after the jet inlet. The incoming high speed air resists the upwards penetration of the jet. This creates a blockage effect, which bends and elongates the jet in the streamwise direction, as seen in Fig. 8.

Fig. 9 compares the mixture fraction contours, along with flow streamlines, on the mid X-Y plane of the combustor for the three cases. In a similar fashion to a bluff-body, the jet acts as an obstacle for the high speed incoming flow, and a region of low pressure is created beyond the first jet. The second jet is placed in this slipstream region of the first jet, which essentially shields the second jet from the high speed incoming flow in the streamwise direction. Due to this shielding effect, the effective jet-to-streamwise momentum ratio of the second injector is increased, which assists in achieving a higher penetration height for the second jet, as seen in Fig. 9. At different second jet positions behind the first jet, different shielding effects can be observed. Once the second jet penetration goes beyond the slipstream region of the first jet, it also bends and elongates in the streamwise direction, due to the blockage effect. It can be observed from the Fig. 9 that the overall height of the mixing boundary is quite dependent on the spacing between the injectors.

Fig. 10 shows the comparison of the P_{norm} isobars and Mach number contours for all 3 cases on the mid X-Y plane of the combustor. It can be seen that the strength and structure of the bow shocks at the second injector is quite different from those of the leading injector and are clearly dependent on the spacing between them.

Fig. 11 shows the evolution of the mixing fraction ϕ over the length of the combustor for Case B. On the bottom X-Z plane in

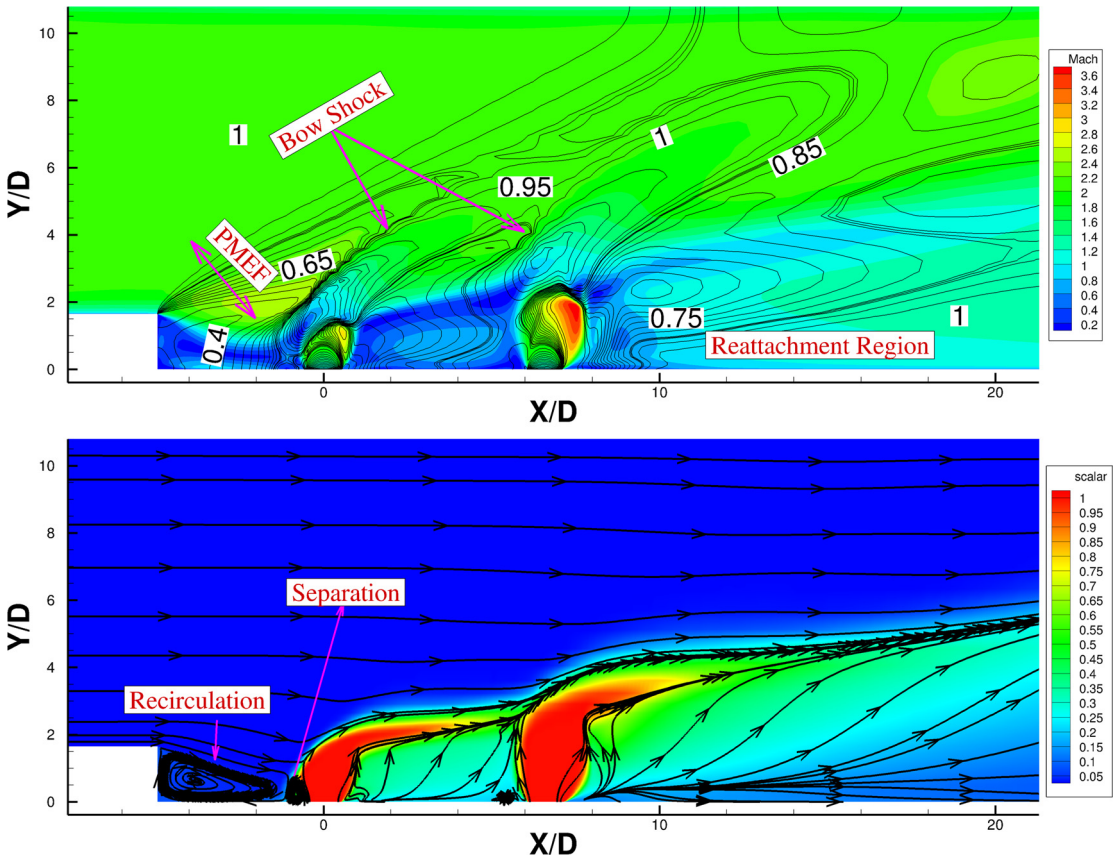

Fig. 8. Top: center-plane P_{norm} isobars with Mach number contours. Bottom: mass fraction of scalar with stream lines.

the figure are shown the contours of the mixing fraction, while the dashed lines represent the 10% and 20% of the injected mixing fraction ϕ at various Y-Z planes. The flow exiting from the injectors is traced by the 3-D streamlines. The counter-rotating vortices cause these streamlines to turn, as seen in the figure. The high speed of the incoming cross-flow bends the streamlines from the injectors, which then align themselves in the direction of the streamwise flow. The high speed of the incoming flow along with absence of any strong convection forces, causes the counter-rotating vortices generated at the injectors to rise. This separation of the injectant jet from the lower wall downstream of the injection is known as jet lift-off [Sharma et al. [14]]. The evolution of the lift-off in the combustor is shown in the Fig. 11, by the dashed contours of the injected mixing fraction ϕ. As the flow moves downstream of the second injector, the size of the 10% and 20% mixing fraction boundaries increase. In the absence of any flow accelerating mechanism (shocks, curvatures, etc.) in the far-field of the second injector, the size of the counter-rotating vortices increase. The jet rises and diffuses laterally, with ϕ values decaying in the streamwise direction. This linear rise of the jet penetration shows that the transverse momentum of the jet is expected as the jet moves further downstream, and the high streamwise momentum of the cross-flow carries the jet forwards and upwards.

4.2. Effect of streamwise vorticity

One of the mechanisms to augment mixing in a SCRAMJET engine is through shock-induced streamwise vorticity. The simplified (i.e. inviscid) equation for vorticity can be given as:

$$\rho \frac{D}{Dt}\left(\frac{\omega}{\rho}\right) = \frac{1}{\rho^2}\nabla\rho \times \nabla P \tag{19}$$

The baroclinic source term in the RHS of the Eqn. (19) shows that the vorticity is generated in a fluid when the pressure and density gradients are non-parallel. When an under-expanded jet at sonic speed is injected in the transverse direction to the incoming flow, it creates a complex flow-field as described in detail by Sharma et al. [24]. The strong bow shock, created in the upstream region of the under-expanded jet, interacts with the jet and creates a strong baroclinic torque. This augments mixing by creating strong streamwise vorticity in the flow field via the source term of Eqn. (19).

Therefore, in order to assess and quantify the effect of streamwise vorticity on the flow-field, the average magnitude of the streamwise vorticity (Γ) is computed over the Y-Z plane of the flow domain which is given as:

$$\Gamma(x) = \iint_{yz} \left| \frac{\partial v}{\partial z} - \frac{\partial w}{\partial y} \right| dydz \tag{20}$$

where the vertical bars indicate absolute values. $\Gamma(x)$ is plotted in Fig. 12 for all the three aforementioned cases and is compared with that of the results of single jet from Sharma et al. [14], which has been referred to as the *baseline case* for all the results presented from here onwards.

For all the three cases, a steep rise in the value of $\Gamma(x)$ is seen in the region preceding the first injector. This rise begins just after the step and reaches a maximum just over the leading jet injection point. For the baseline case, the $\Gamma(x)$ decreases monotonically after the injection point at $X/D = 0$, but for the dual jet configurations, a steep rise is again seen in the vicinity of the second injector. The peak value of $\Gamma(x)$ at the leading injector is same for all the 3 cases, but the height of the second peak of $\Gamma(x)$ decreases with increase in the spacing for the second injector. It should also

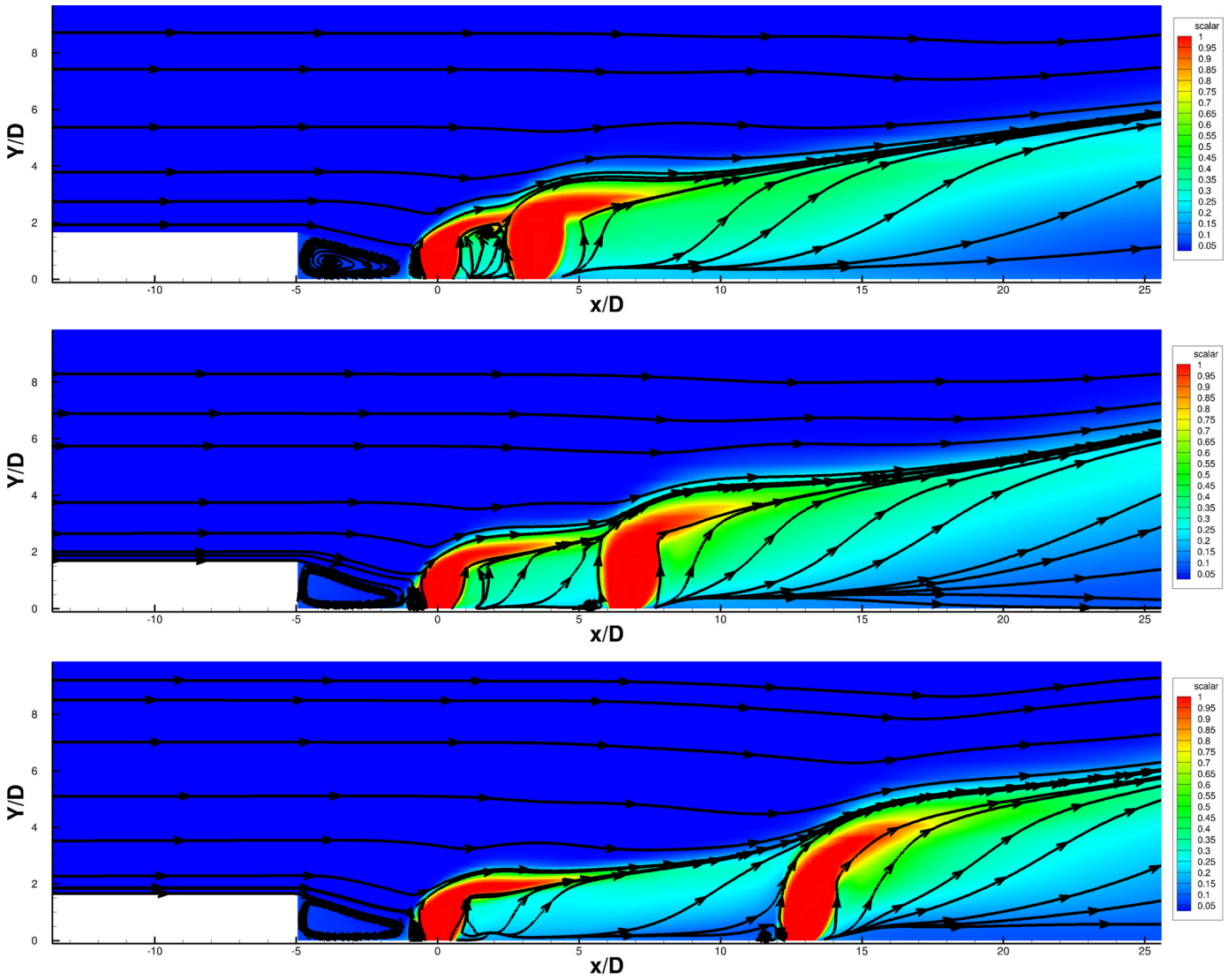

Fig. 9. Comparison of Center-plane scalar mass fractions with streamlines for Case A, B and C respectively.

be noted that all the cases closely follow the results of the baseline case until the vicinity of the second injector, wherever that is located.

For Case A, as the injectors are located quite close to each other, and in the momentum zone, the streamwise vorticity generated at the first injector is then further enhanced by the follow-up injector. This results in an increase in the peak value of $\Gamma(x)$, resulting in further enhancement the lateral convection present in this region. For Case B, the streamwise vorticity starts to decay after the leading injector, and follows the baseline case pattern up until the second injector, which then increases the lateral convection in the flow field. It should be noted that the injector in Case B is placed in the intermediate zone of transition from the momentum to diffusion dominated flow, and the magnitude of streamwise vorticity rises to the levels nearly comparable to the Case A. In Case C, the second injector is placed in the diffusion zone of the mixing boundary. The rise in peak value of $\Gamma(x)$ for second injector in Case C is similar to that of the leading injector. From Fig. 12 it is evident that the greatest increase in average vorticity over the length for $X/D = 0$ to 25 is in Case A, followed by B and C. Thus Case A presumably gives the best results from the view point of mixing.

4.3. Mixing characteristics

The mixing fraction ϕ is tracked to observe mixing between the incoming streamwise flow and the fuel jet. Fig. 13 shows the mixing characteristics for the three different spacings between the injectors compared with single injector case from Sharma et al. [14] that is marked as the baseline case. The jet penetration and spread, which are shown in Fig. 13a and 13b respectively, are defined as the boundaries where the ϕ value reaches 1% of the $\phi_{max}(=1)$ of the jet inlet. Fig. 13c shows the maximum mass fraction of the scalar ϕ in the jet-penetration region shown in Fig. 13a. It is seen from Fig. 13 that the initial trend of mixing characteristics is similar to that of the baseline case, with abrupt changes in the vicinity of the second injector. In Case A, with the injectors quite close to each other, a longer lateral momentum dominated region is obtained. Compared to the baseline case, followed by a diffusion zone observed in Fig. 13a at $X/D > 10$, where the penetration becomes linear in the streamwise direction. The presence of higher streamwise momentum of the first jet over the second injector, due to the bending of the fuel jet into the streamwise direction (see Fig. 9), creates a blocking effect for the second jet resulting in the least jet penetration of all the 2-jet cases. The peak penetration height is achieved after the second injector. In Case B,

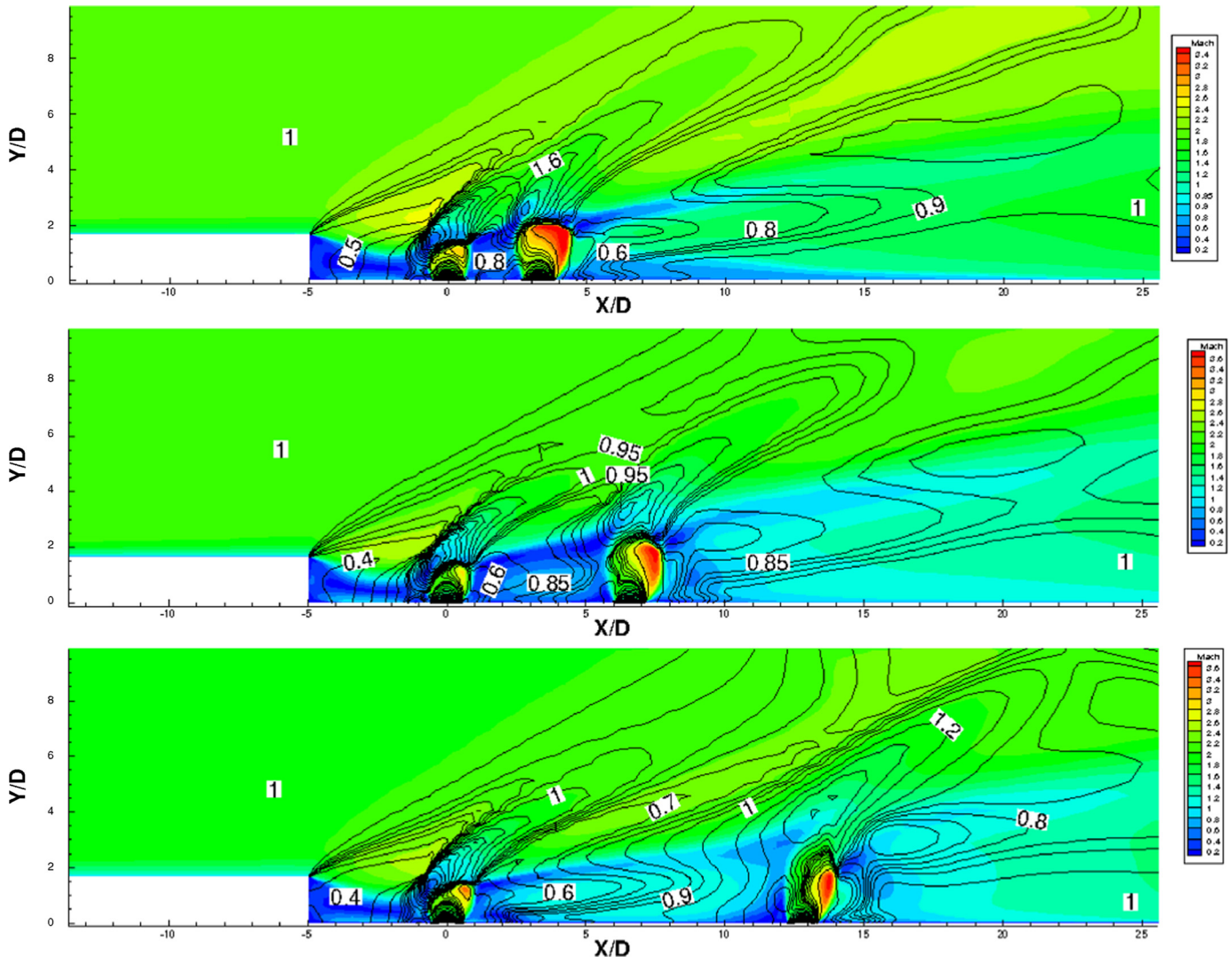

Fig. 10. Comparison of Center-plane P_{norm} isobars and Mach number contours for Case A, B and C respectively (top to bottom).

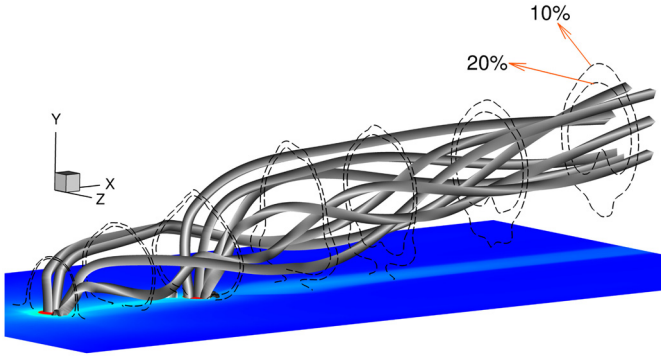

Fig. 11. Plot showing 3-D evolution of streamlines along with mixture fraction ϕ on Y-Z plane plotted from $X/D = 0$ at every interval of $X/D = 2$ for Case B.

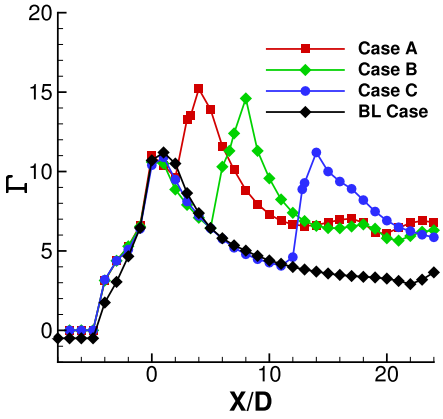

Fig. 12. Average magnitude of the streamwise vorticity in the Y-Z plane.

since the injector is placed in the transition zone, the streamwise momentum of the first jet over the location is less than that of Case A, which helps in increasing the penetration height. In Case C, since the second injector is placed in the diffusion zone, a steep rise in penetration height can be seen which pushes the jet penetration boundary furthermost of the three cases. The horizontal spread of the mixing region jets shown in Fig. 13b exhibits similar results to the jet penetration. The spread is steep near the first injector, which then further increases in the vicinity of the second injector. In the diffusion region, the spreading stops and the jet width becomes essentially constant. Considered quantitatively, the volumes of the mixing zone are approximately same in cases A and B, with the jet penetration and spread in the second case increasing somewhat after the first, but to greater values. But in case C, the volume of mixing zone is smaller, due to the delayed increases.

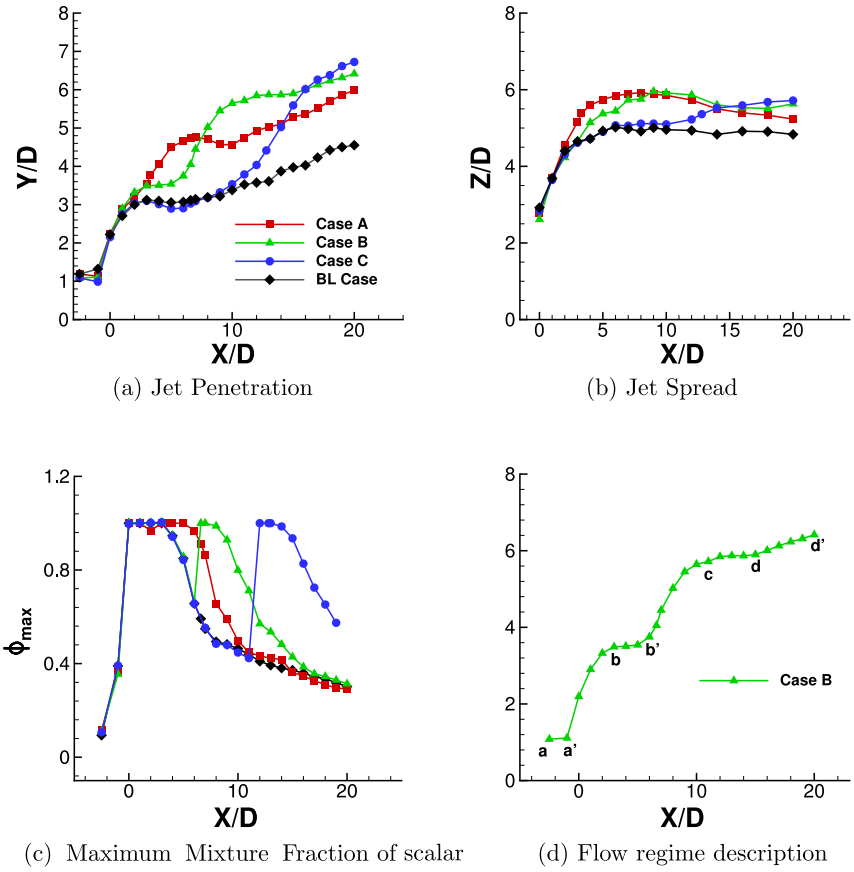

(a) Jet Penetration (b) Jet Spread

(c) Maximum Mixture Fraction of scalar (d) Flow regime description

Fig. 13. Mixing characteristics.

The maximum mass fraction of ϕ in the mixing zone, is shown in Fig. 13c. It can be presumed that a higher value of ϕ_{max} indicates poorer mixing. From the figure, it can be seen that the ϕ gradually decays after the first injector, but is then again replenished by the second injector, leading to again reaching the value of $\phi_{max} = 1$ in all the three cases. For Case A in Fig. 13c, it is observed that as the injector is placed in the momentum zone, it leads to a continuous region of $\phi_{max} = 1$ from $X/D = 0$ to $X/D \approx 6$, after which there is decay in the values of ϕ_{max}. In this arrangement the core of the jets remains unmixed in the momentum zone, beyond which it steeply decreases. On other hand, in Cases B and C, the leading jet decays to lower values till $X/D \approx 5, 10$ respectively, after which it is replenished by the second injector, before decaying again. It can be observed that by the end of the domain, cases A and B have almost identical decay of ϕ_{max}, but case C has significantly higher values, indicating poorer mixing.

Fig. 13d shows the division of the flow into various regimes on the jet penetration graph for Case B. Region from a' to a, represents the flow preceding the first injector. A sharp rise in the value of jet penetration between a and b represents the lateral momentum zone, which exists till $X/D \approx 3$. After location b, the penetration boundary remains almost constant till the region in the vicinity of upstream of the second injector, which is denoted by point b'. Due to the second injector, another steep increase in penetration boundary can be noted from b' to c due to the lateral convection effects. The shielding effect of the first jet helps in achieving a higher penetration height at the second injector. After the location c, the penetration boundary flattens till point d falls and then begins to rise linearly beyond d due to lateral diffusion.

4.4. Loss of stagnation pressure

The function of the SCRAMJET engine is to produce thrust. A higher exit velocity will result in higher thrust from the engine, hence minimum stagnation pressure loss between the inlet and the exit is desirable. The transverse fuel injection configuration produces substantial loss in stagnation pressure, due to the presence of strong shocks in the flow field. Therefore, to characterize this loss in a SCRAMJET engine, we define the mass-flow-weighted-average of the stagnation pressure (p_0) in the Y-Z plane as:

$$P_0(x) = \iint_{yz} p_0 \rho u \, dy \, dz \Big/ \iint_{yz} \rho u \, dy \, dz \tag{21}$$

subsequently normalized as $P_{0,norm}$ by dividing $P_0(x)$ by the stagnation pressure at the inlet. Fig. 14 shows the loss in normalized stagnation pressure for the three cases with dual injectors, along with the baseline case results. With the first jet injection, a steep decrease in values of $P_{0,norm}$ in the near-upstream and downstream of the injector ($X/D > 0$) is observed due to the presence of the bow shocks due to the injection. A higher loss in P_0, norm shows presence of stronger shock strength. The second injector introduces more shocks in the combustor, leading to higher loss in $P_{0,norm}$. A further decrease in the value of $P_{0,norm}$ for all the dual jet cases can be attributed to the bow shocks that are formed in front of the second injector, variously located, which is absent in the baseline case.

Although the difference in the $P_{0,norm}$ between the three cases is small, it is observed the loss in $P_{0,norm}$ increases with increase in spacing between the jets. These results show that as the spacing between the jets is increased, the bow shock generated by the

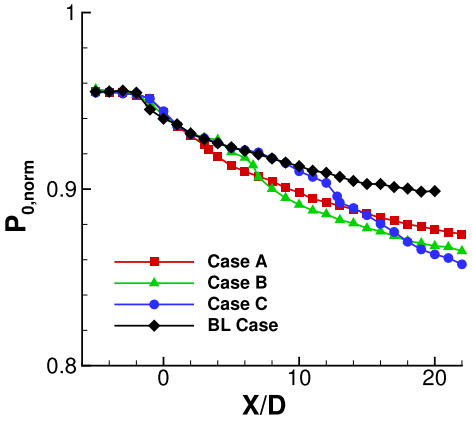

Fig. 14. Normalized stagnation pressure distribution in Y-Z plane.

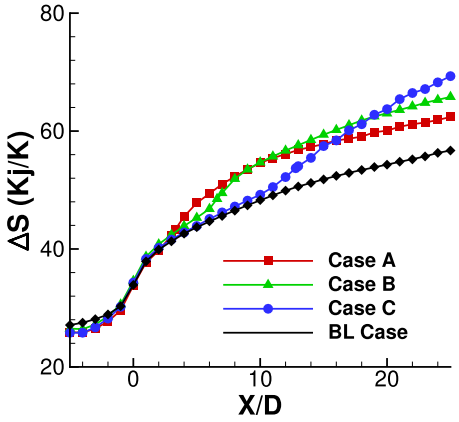

Fig. 15. ΔS distribution in Y-Z plane.

second injector becomes stronger. Thus Case A is the best of the three cases, in terms of pressure loss, followed by Case B and C.

4.5. Rise in entropy

Rise in the entropy of a system represents the total amount of energy unavailable to do work due to irreversible processes. Therefore, a greater rise in entropy will result in a less efficient system. The change in entropy (ΔS) in the computational domain at every cell center c is computed using Gibb's law as:

$$\Delta S_c = C_p \, ln(T_{norm}) - R \, ln(P_{norm}) \tag{22}$$

where the reference state is taken as the inlet condition. The loss ΔS in the SCRAMJET combustor rises primarily due to (a) mixing of the jet and air and (b) due to presence of various shocks in the system. The average entropy in the Y-Z plane is then evaluated as the mass flow weighted average as:

$$\Delta S(x) = \iint_{yz} (\Delta S_c) \rho u \, dy \, dz \Big/ \iint_{yz} \rho u \, dy \, dz \tag{23}$$

Fig. 15 shows the rise in entropy for the three cases of the dual-jet combustor compared with the baseline case. It is observed that entropy increases even before the first injection, i.e. $\Delta S > 0$, due to the entropy gain due to the PMEF and re-compression shocks after the sudden expansion of the step (P2). The steep rise in entropy at the leading injector is present for all 3 cases, which is similar to the baseline case. This rise in ΔS can be attributed to the bow shocks before the first injector. The plot of ΔS exhibits a sharp rise around second injector, which results in higher ΔS for all three cases compared to the baseline case. As no or very weak shock structures are present in the region of decay of the mixing region (beyond the second injector), the ΔS keeps increasing only due to the mixing and the graph becomes almost linear. This suggests that the Case A is the most thermodynamically efficient, followed by Case B and C.

5. Conclusions

To optimize the design and performance of a dual-jet SCRAMJET engine, an optimal spacing between the fuel injectors is desired. In this work, a SCRAMJET combustor with two transverse fuel jet injectors having an upstream backward facing step as a flame holder has been studied. The study involves no combustion, as it has been suggested by previous works [15–17] that supersonic flow and combustion are quite decoupled in this situation, implying that even cold-flow optimization would be a good first approximation to the actual combustor problem. The study is conducted using our in-house 3D parallel RANS unstructured grid solver. Menter's low-Reynolds number SST model has been used to resolve turbulence. Appropriate validations for the code and the model have been presented.

The baseline case for the study has been chosen from Sharma et al. [14] as single injector optimally located at the reattachment point of the recirculation zone in the downstream of the backward step. The results for the baseline case show that the flow-field can be divided into three distinct flow regions downstream of the leading injector. The leading injector is kept fixed as per the results of Sharma et al. [14] and the second injector is then placed in each of these three flow regions in separate simulations, forming three cases for study. These three regions can be described as follows: (a) immediately after the first injector, the jet penetration into the streamwise flow is strongly affected by the transverse momentum of the jet. This is called the "momentum zone" (b) after which, the jet penetration remains relatively constant over a short distance called the "transition zone" and (c) then increase linearly with the streamwise distance by lateral diffusion in the "diffusion zone". The second jet is placed in each of the zones to form the Cases A, B and C of the study.

It is observed that the SCRAMJET performance and mixing of air-fuel stream is directly affected by the spacing between the injectors. In order to quantify this influence and its effect on performance, various parameters were studied, for which results have been presented. It is observed that all the flow quantities remain quite close to the baseline case results till the near-field of the second injector, irrespective of its location in the flow field results. This shows (as expected in supersonic flows) that while the leading injector affects the flow features of the second injector the upstream flow is not influenced by the injector located downstream. As the spacing between the injectors in increased, the average magnitude of streamwise vorticity decreases. It can be reasonably presumed that the higher streamwise vortictiy directly correlates with better mixing. The value of the second peak value of average magnitude of streamwise vorticity decreases with increase in spacing between the jets. The average streamwise vorticity over the region $X/D = 0$ to 25, after the first injector shows a similar trend – with values decreasing with injector distance. Thus Case A gives best mixing followed by Case B and C.

In the study of jet penetration and spread, it is observed that there is a sharp increase in both the leading jet, and then again at the second jet, whatever its location. Greater increase in both are achieved the further downstream the second jet is located. But earlier location causes the second jet to have influence over a longer distance downstream. Qualitatively, the volumes of the mixing zone are comparable for Cases A and B, while Case C is definitely inferior to the others by this measure. It is found that

the loss in stagnation pressure and entropy increases with increase in the spacing between the fuel jets. These results can be traced to the increase in the strength of the bow shock as the spacing is increased. As the strength of the shocks in the system increases with increase in spacing between the injectors, the thermodynamic efficiency of the combustor decreases. So, with respect to these thermodynamic measures of performance, Case A is the best, followed by B and C.

It should be noted that while a flame holder is present for the first jet (in form of the backward facing step in the combustor) a physical mechanism for holding the flame after ignition is missing for the second jet (or any number of jets placed in the downstream of the first jet), which would make it quite difficult to ignite and hold the flame, if the jets are placed at a considerable distance from each other, such as in Case C. The shielding effect due to the first jet in Case A and B would protect the flame from getting extinguished; but if the jets are placed too close to each other, it could very well lead to large amount of localized heat generation that could adversely affect the wall temperature of the combustor.

For almost all the considerations of performance – jet penetration and spread, streamwise vorticity, stagnation pressure, streamwise vorticity, stagnation pressure loss, entropy increase – it is found that Case A is best followed by B and C, The sole exception to this for the jet penetration where the best case is C, followed by B and A. However, even this is arguable, as Fig. 13a shows the jet penetration increases earliest for A, to be overtaken only downstream by B and C.

So, the best location for the second injector from almost all considerations is Case A. This location is at the end of the momentum zone ($X/D = 3.3$), where the transverse momentum of the first jet is expended and further jet penetration and spread is extended, after a transition zone, by diffusion.

Declaration of competing interest

This research did not receive any specific grant from funding agencies in public, commercial or not-for-profit sectors. The authors declare that they have no conflict of interest.

References

[1] S. Aso, S. Okuyama, Y. Ando, T. Fujimori, Two-dimensional and three-dimensional mixing flow fields in supersonic flow induced by injected secondary flows through traverse slot and circular nozzle, in: 31st Aerospace Sciences Meeting, AIAA, Reno, NV, U.S.A., 1993, p. 489.

[2] W. Huang, L. Yan, Progress in research on mixing techniques for transverse injection flow fields in supersonic crossflows, J. Zhejiang Univ. Sci. A 14 (8) (2013) 554–564, https://doi.org/10.1631/jzus.A1300096.

[3] S. Chen, D. Zhao, RANS investigation of the effect of pulsed fuel injection on scramjet HyShot II engine, Aerosp. Sci. Technol. 84 (2019) 182–192, https://doi.org/10.1016/j.ast.2018.10.022.

[4] J.C. McDaniel, J. Raves, Laser-induced-fluorescence visualization of transverse gaseous injection in a nonreacting supersonic combustor, J. Propuls. Power 4 (6) (1988) 591–597, https://doi.org/10.2514/3.23105.

[5] J. Mcdaniel, D. Fletcher, R. Hartfield, S. Hollo, Transverse injection into Mach 2 flow behind a rearward-facing step - A 3-D, compressible flow test case for hypersonic combustor CFD validation, https://doi.org/10.2514/6.1991-5071, 1991, p. 5071.

[6] A. Karagozian, K. Wang, A.-T. Le, O. Smith, Transverse gas jet injection behind a rearward-facing step, J. Propuls. Power 12 (6) (1996) 1129–1136, https://doi.org/10.2514/3.24153.

[7] D. Chakraborty, A. Roychowdhury, V. Ashok, P. Kumar, Numerical investigation of staged transverse sonic injection in Mach 2 stream in confined environment, Aeronaut. J. 107 (1078) (2003) 719–729, https://doi.org/10.1017/S0001924000013476.

[8] A. Sriram, D. Chakraborty, Numerical exploration of staged transverse injection into confined supersonic, Def. Sci. J. 61 (1) (2011) 3–11, https://doi.org/10.14429/dsj.61.20.

[9] A. Oamjee, R. Sadanandan, Fuel injection location studies on pylon-cavity aided jet in supersonic crossflow, Aerosp. Sci. Technol. 92 (2019) 869–880, https://doi.org/10.1016/j.ast.2019.07.021.

[10] W. Li, H. Liu, Large-eddy simulation of shock-wave/boundary-layer interaction control using a backward facing step, Aerosp. Sci. Technol. 84 (2019) 1011–1019, https://doi.org/10.1016/j.ast.2018.11.005.

[11] A.S. Pudsey, R.R. Boyce, Numerical investigation of transverse jets through multiport injector arrays in a supersonic crossflow, J. Propuls. Power 26 (6) (2010) 1225–1236, https://doi.org/10.2514/1.39603.

[12] M.B. Gerdroodbary, M.R. Takami, H. Heidari, K. Fallah, D. Ganji, Comparison of the single/multi transverse jets under the influence of shock wave in supersonic crossflow, Acta Astronaut. 123 (2016) 283–291, https://doi.org/10.1016/j.actaastro.2016.03.031.

[13] W. Huang, Y. Li, L. Yan, R. Moradi, Mixing enhancement mechanism induced by the cascaded fuel injectors in supersonic flows: a numerical study, Acta Astronaut. 152 (2018) 18–26, https://doi.org/10.1016/j.actaastro.2018.07.027.

[14] V. Sharma, V. Eswaran, D. Chakraborty, Computational analysis of transverse sonic injection in supersonic crossflow using Rans models, ASME J. Fluids Eng. (January 1, 2020), https://doi.org/10.1115/1.4045985.

[15] V. Ton, A. Karagozian, F. Marble, S. Osher, B. Engquist, Numerical simulations of high-speed chemically reacting flow, Theor. Comput. Fluid Dyn. 6 (2–3) (1994) 161–179, https://doi.org/10.1007/BF00312347.

[16] S.-H. Lee, I.-S. Jeung, Y. Yoon, Computational investigation of shock-enhanced mixing and combustion, AIAA J. 35 (12) (1997) 1813–1820, https://doi.org/10.2514/2.56.

[17] S.-H. Lee, I.-S. Jeung, Y. Yoon, Computational investigation of shock-enhanced mixing: application to circular cross section combustor, AIAA J. 36 (11) (1998) 2055–2062, https://doi.org/10.2514/2.306.

[18] J.M. Weiss, W.A. Smith, Preconditioning applied to variable and constant density flows, AIAA J. 33 (11) (1995) 2050–2057, https://doi.org/10.2514/3.12946.

[19] F.M. White, I. Corfield, Viscous Fluid Flow, vol. 3, McGraw-Hill, New York, 2006, pp. 67–73, Ch. 2.

[20] J.M. Weiss, J.P. Maruszewski, W.A. Smith, Implicit solution of preconditioned Navier-Stokes equations using algebraic multigrid, AIAA J. 37 (1) (1999) 29–36, https://doi.org/10.2514/2.689.

[21] P.L. Roe, Approximate Riemann solvers, parameter vectors, and difference schemes, J. Comput. Phys. 43 (2) (1981) 357–372, https://doi.org/10.1016/0021-9991(81)90128-5.

[22] V. Venkatakrishnan, On the accuracy of limiters and convergence to steady state solutions, in: 31st Aerospace Sciences Meeting, AIAA, Reno, NV, U.S.A., 1993, p. 880.

[23] V. Venkatakrishnan, Convergence to steady state solutions of the Euler equations on unstructured grids with limiters, J. Comput. Phys. 118 (1) (1995) 120–130, https://doi.org/10.1006/jcph.1995.1084.

[24] V. Sharma, V. Eswaran, D. Chakraborty, Computational analysis of transverse sonic injection in supersonic crossflow using rans models, unpublished results, 2019.

[25] F.R. Menter, Two-equation eddy-viscosity turbulence models for engineering applications, AIAA J. 32 (8) (1994) 1598–1605, https://doi.org/10.2514/3.12149.

[26] I.B. Celik, U. Ghia, P.J. Roache, Procedure for estimation and reporting of uncertainty due to discretization in cfd applications, J. Fluids Eng. 130 (7) (2008), https://doi.org/10.1115/1.2960953.